Article:
Yu, J., Kasama, K., Yuan, R. et al. (2026) Post-failure analysis of layered slope considering strength spatial variability using GPU-accelerated random material point method. Advances in Engineering Software, 218. 104171. ISSN: 0965-9978

https://doi.org/10.1016/j.advengsoft.2026.104171

Post-failure analysis of layered slope considering strength spatial variability using GPU-accelerated random material point method

Junyan Yu [a, b], Kiyonobu Kasama [b, *], Ran Yuan [a, c], Chong Peng [d], Yongxing Wang [e], Abdulqader M. Mohsen Al-Abadi [f], Yi He [c, g, *]

[a] School of Civil Engineering, Southwest Jiaotong University, Chengdu, 610031, China.

[b] Department of Civil Engineering, Kyushu University, Fukuoka, 819-0395, Japan.

[c] Key Laboratory of High-speed Railway Engineering, Ministry of Education, Southwest Jiaotong University, Chengdu, 610031, China.

[d] School of Civil Engineering, Southeast University, Nanjing 211189, China.

[e] School of Computer Science, University of Leeds, Leeds, LS2 9JT, UK.

[f] Faculty of Computing and Information Technology, University of Aden, Aden, 6312, Republic of Yemen.

[g] Faculty of Geosciences and Engineering, Southwest Jiaotong University, Chengdu, 611756, China.

[*] Corresponding author.

Abstract:

Soil within natural slopes exhibits heterogeneity characterized by stratification and spatial variability of material properties. Nevertheless, existing large-deformation analyses that account for strength spatial variability have predominantly been conducted using single-layer slope models or have focused solely on undrained conditions. Such simplifications limit the ability to capture realistic landslide hazards of layered slopes. To investigate how coupled spatial variability of cohesion (c) and internal friction angle (φ), together with stratification, jointly governs post-failure behaviors and failure modes of landslides, this study performs stochastic large-deformation analyses of two-layer slopes by integrating random field theory. A GPU-accelerated Random field Material Point Method (GPU-RMPM) framework is developed to enable efficient large-scale Monte Carlo simulations (MCSs). Parameter sensitivity analyses are conducted to examine the effects of horizontal scale of fluctuation (θ_h), coefficient of variation (COV), the rotation angle of anisotropy (β), and the cross-correlation coefficient ($R_{c\varphi}$) between c and φ on post-failure behaviors and failure modes. The results show that shear strength spatial variability gives rise to distinct

local failure (LF) and global failure (GF) modes. The GF mode mobilizes a larger sliding volume than the LF mode under a comparable influence range. Moderate horizontal heterogeneity amplifies the variability of post-failure behaviors, whereas sufficiently large θ_h lead to homogenized behavior and reduced uncertainty. Increasing COV and $R_{c\varphi}$ substantially enlarge both the mean values and variability of influence range and sliding volume, increasing the likelihood of extreme scenarios. The GPU-RMPM framework achieves approximately tenfold speedup over conventional CPU-based approaches, enabling practical stochastic large-deformation analyses.

Keywords: Layered slope; Large-deformation analysis; Strength spatial variability; GPU parallel acceleration; Random material point method

Introduction

Soil within natural slopes forms inherently heterogeneous systems arising from depositional environments, weathering processes, and long-term geological evolution. One of the most prominent manifestations of this heterogeneity is soil stratification, whereby distinct soil layers with different mechanical characteristics are formed over geological time [1-3]. Extensive studies in slope stability analysis have demonstrated that stratified (layered) slopes exhibit more complex failure mechanisms and require more sophisticated evaluation approaches than single-layer slopes [4,5]. Using simplified single-layer models to assess layered slopes may therefore lead to an underestimation of instability and associated hazard potential [6]. These findings highlight the critical role of stratification in governing stability analysis of pre-failure slope. In contrast, investigations of post-failure large-deformation behaviors—which directly controls landslide damage severity—have predominantly been conducted using single-layer slope models [7,8]. Such simplifications are often introduced to reduce computational complexity or to facilitate methodological development, rather than to reflect realistic geological conditions. Although these studies have provided valuable insights into post-failure landslide hazard assessment, this inconsistency raises a fundamental question: whether conclusions drawn from large-deformation analyses of single-layer slopes remain valid for practical layered slopes? Addressing this question is essential; therefore, a systematic investigation that explicitly accounts for soil stratification is required to improve the reliability and realism of landslide hazard assessments.

Beyond stratification, spatial variability of material properties represents another fundamental scale of heterogeneity in soils forming natural slopes. Even within an individual soil layer, soil properties exhibit continuous spatial fluctuations. This intra-layer heterogeneity is commonly characterized using random field theory, which provides a quantitative framework for incorporating spatial variability into numerical analyses [9-11]. Previous large-deformation studies have demonstrated that statistical parameters of random fields—including the coefficient of variation (COV), scale of fluctuation, and the cross-correlation coefficient ($R_{c\varphi}$) between cohesion (c) and internal friction angle (φ)—can significantly influence post-failure behaviors, such as runout distance, influence range, and sliding volume [12,13]. For instance, increasing COV has been shown to amplify the probability and magnitude of extreme post-failure outcomes [14], while variations in scale of fluctuation affect the continuity of weak zones and the formation of failure surfaces [15]. In addition, the $R_{c\varphi}$ has been reported to alter post-failure behaviors [16]. Most existing investigations, however, assume isotropic or transverse anisotropic auto-correlation structures, in which spatial correlations are aligned with the horizontal and vertical directions. Nature soil deposits often exhibit inclined stratification and spatial auto-correlation structures that are rotated with respect to the principal geometric axes—referred to as rotated anisotropy [17]. Recent studies by Bi et al. [18], Li et al. [19] and Jiang et al. [20] have explored the influence of rotated anisotropy on post-failure behaviors using single-layer slope models. Nevertheless, to the authors' knowledge, the effects of rotated anisotropic spatial variability on post-failure behaviors of layered slopes have not yet been systematically investigated. This limitation constrains current understanding of how spatial variability interacts with stratification in post-failure large-deformation analysis.

The consideration of layered slope models introduces additional mechanical complexity. Compared to single-layer slope failure mechanisms [21,22], soil stratification facilitates multiple competing failure mechanisms to develop [3,23], thereby making post-failure behaviors highly sensitive to the spatial distribution of soil strength. Existing stochastic large-deformation studies that consider layered slopes have often simplified the problem by assuming spatial variability in c only, particularly under undrained conditions [24]. Although such assumptions facilitate numerical implementation and reduce computational cost, they inherently constrain the range of failure mechanisms that can be captured. In many practical slope engineering scenarios, soils experience sufficient time for drainage and consolidation, and the φ becomes a governing parameter controlling shear resistance and energy dissipation during large-deformation processes [25,26]. Reliability-based studies have consistently demonstrated that spatial variability in φ plays a critical role in influencing failure probability and failure modes (local failure and

global failure) [27-30]. These findings suggest that neglecting the spatial variability of φ may lead to an incomplete or biased representation of slope failure mechanisms. However, incorporating φ spatial variability into stochastic large-deformation analysis is substantially more challenging than in conventional reliability analysis, since modeling both c and φ as spatially variable random fields significantly increases both the stochastic dimensionality and the coupling complexity of the strength parameters. In addition, large-deformation responses are highly nonlinear and strongly realization-dependent [8,31]. Different random field realizations may activate distinct failure modes, leading to pronounced variability in influence range and sliding volume. Consequently, a large number of computationally expensive large-deformation simulations are required to obtain statistically meaningful results. Owing to these challenges, the coupled c-φ spatial variability has not yet been systematically incorporated into stochastic large-deformation analyses of layered slopes.

Large-deformation analyses of slopes have been investigated using various numerical approaches, including the smoothed particle hydrodynamics (SPH) [32-35], discrete element method (DEM) [36], and material point method (MPM) [37,38]. Among these methods, MPM has been widely adopted in slope engineering because boundary conditions can be imposed more conveniently than in SPH, while its computational demand is generally lower than that of DEM. Nevertheless, MPM remains computationally intensive even for a single large-deformation simulation, and the computational burden becomes substantially greater when stochastic analysis is introduced. Several probabilistic frameworks have attempted to alleviate this difficulty by adopting hybrid strategies (e.g., RLEM-RMPM [24], RFEM-RMPM [39]), in which only the predicted failure cases are subsequently subjected to large-deformation simulations. However, these hybrid strategies are primarily designed to complement reliability analysis. While they ensure statistical convergence of failure probability, they do not necessarily guarantee reliable characterization of realization-dependent large-deformation behaviors in a random field framework [7]. Consequently, a sufficiently large number of Monte Carlo simulations (MCSs) is required to achieve statistically convergent characterization of post-failure landslide processes [40,41]. The combined consideration of soil stratification, coupled c-φ spatial variability, large-deformation analysis, and MCSs thus poses a severe computational efficiency challenge [42]. To address such high-dimensional and computationally demanding problems, various advanced strategies have been developed in recent years, including surrogate modeling techniques [43-46], machine learning approaches [47], and GPU-based parallel computing [48]. Among them, GPU-based parallel acceleration has demonstrated particular potential in computational mechanics and has been successfully applied to large-deformation numerical simulations

[49], significantly enhancing computational efficiency while preserving physical fidelity. With the rapid development and widespread adoption of GPUs in scientific computing, this approach provides a viable pathway to overcome the computational bottleneck that has thus far limited stochastic large-deformation analyses of layered slopes.

To address the above challenges, this study develops and applies a GPU-accelerated random material point method (GPU-RMPM) to investigate post-failure behaviors and failure modes of stratified slopes considering the coupled spatial variability of c and φ. The proposed framework enables statistically converged MCSs that would otherwise be computationally prohibitive, while retaining the capability to resolve nonlinear large-deformation landslide processes. This study provides new insights into how strength spatial variability and soil stratification jointly govern post-failure landslide hazards. The main innovations and contributions of this study are summarized as follows: (1) A GPU-parallelized RMPM framework is developed to significantly enhance the computational efficiency of stochastic large-deformation analysis, making statistically converged MCSs feasible for post-failure landslide simulations. (2) A stochastic large-deformation modeling framework is established that explicitly incorporates both soil stratification and coupled c-φ spatial variability, thereby extending existing probabilistic slope analyses beyond conventional stability approaches. (3) The influences of key spatial variability parameters—including horizontal scale of fluctuation (θ_h), COV, rotation angle of anisotropy (β), and $R_{c\varphi}$—on failure mode evolution and post-failure hazard magnitude are systematically quantified, revealing the mechanisms by which geological uncertainty controls landslide consequences.

Methodology

Auto-correlation structure

Random Field Theory (RFT) is a mathematical framework used to describe the uncertainty of spatial variables, widely applied in geotechnical engineering to investigate the spatial variability of soil properties [50]. In RFT, soil properties are generally treated as random variables, whose distribution follows a predefined probability density function, commonly Gaussian distribution (normal distribution) or non-Gaussian distribution (lognormal distribution). However, values within the random field must satisfy a predefined spatial correlation structure, which is governed by an $n \times n$ autocorrelation matrix $\boldsymbol{C}$:

$$\boldsymbol{C} = \begin{bmatrix} 1 & \rho_c(x_1, x_2) & \cdots & \rho_c(x_1, x_n) \\ \rho_c(x_2, x_1) & 1 & \cdots & \rho_c(x_2, x_n) \\ \vdots & \vdots & \ddots & \vdots \\ \rho_c(x_n, x_1) & \rho_c(x_n, x_2) & \cdots & 1 \end{bmatrix} \quad 12\text{* MERGEFORMAT ()}$$

In a discretized random field, n represents the number of elements used to discretize the spatial domain. The spatial correlation between any two points i and j within the field is characterized by the autocorrelation coefficient $\rho_c(xi, xj)$, which is determined by the specific form of the autocorrelation function (ACF). Owing to complex geological deposition and depositional processes, soil deposits may exhibit a variety of spatial structures, including isotropy, transverse anisotropy, and rotated anisotropy [17]. In the present study, spatial variability of soil properties is modeled using the single exponential ACF [9], which has been widely applied in geotechnical random field analyses due to its simplicity and robustness. The corresponding autocorrelation function is expressed as follows:

$$\rho_c(\tau_x, \tau_y) = \exp\left(- \frac{\left| \tau_x \cos\beta + \tau_y \sin\beta \right|}{\theta_h} - \frac{\left| -\tau_x \sin\beta + \tau_y \cos\beta \right|}{\theta_v} \right) \quad 34\text{* MERGEFORMAT ()}$$

where τ_x and τ_y are the distances between any two points in space along the horizontal (X) and vertical (Y) directions, respectively; θ_h and θ_v represent the scales of fluctuation in the horizontal and vertical directions, respectively. β denotes the rotation angle of anisotropy to the principal axis. When $\theta_h = \theta_v$, it means the isotropy of soil spatial variability. When $\theta_h \neq \theta_v$ and $\beta = 0°$, it means the transverse anisotropy of soil spatial variability.

Discretization method for the random field

The autocorrelation matrix $\boldsymbol{C}$ defines how values at different spatial locations are correlated, ensuring that the generated random field realistically captures the natural heterogeneity of the soil. Once the $\boldsymbol{C}$ is determined, it is typically processed using numerical techniques such as Karhunen-Loève expansion or Cholesky Matrix Decomposition (CMD) to generate realizations of the random field. These realizations are essential for MCS, where multiple random field samples are generated to account for the statistical variability of soil properties in slope deformation analyses. For CMD, $\boldsymbol{C}$ can be decomposed into a lower triangular matrix $\boldsymbol{L}_1$ and its conjugate transpose $\boldsymbol{L}_1^T$ as follows:

$$C = L_1 \cdot L_1^T$$ 56* MERGEFORMAT ()

with this decomposition, the random field $\boldsymbol{H}_{xi}$ can be numerically generated using:

$$H_{xi} = L_1 \cdot \xi_{xi} \quad (xi = c, \varphi)$$ 78* MERGEFORMAT ()

ξ_{xi} is a vector of independent standard normal random variables.

The corresponding cross-correlation matrix $\boldsymbol{R}$ can be obtained based on cross-correlation coefficient $R_{c\varphi}$ between c and φ as follows:

$$\boldsymbol{R} = \begin{bmatrix} R_{cc} & 0 \\ 0 & R_{\varphi\varphi} \end{bmatrix}$$ 910* MERGEFORMAT ()

The CMD of the cross-correlation matrix $\boldsymbol{R}$ obtains the corresponding lower triangular matrix $\boldsymbol{L}_2$, which in turn derives the cross-correlated Gaussian random fields of c and φ:

$$H_{xi}^{CR} = H_{xi} \cdot L_2^T$$ 1112* MERGEFORMAT ()

Finally, based on the statistical characteristics (i.e., mean value, COV, and marginal distribution) of the soil parameters, the cross-correlated Gaussian random field realization is transformed through equiprobable transformation to obtain the cross-correlated non-Gaussian random field realization as follows [51]:

$$H_{xi}^{NG} = F^{-1}\left[\Phi(H_{xi}^{CR})\right]$$ 1314* MERGEFORMAT ()

where $\Phi(\cdot)$ is the cumulative distribution function (CDF) of a standard normal variable; $F^{-1}(\cdot)$ is the inverse CDF of the marginal distribution of $\boldsymbol{H}_{xi}$.

GPU-accelerated Random Field MPM (GPU-RMPM)

The MPM is a numerical method that combines the strengths of Lagrangian and Eulerian descriptions [52]. It is particularly effective for modeling problems involving large deformations, contact, and mass flow. MPM discretizes the continuum body into a set of material points (particles) that carry all physical quantities such as mass, velocity, stress, and strain. These particles interact through a background computational grid, which is reset each time step to avoid mesh distortion. MPM includes particle-to-grid (P2G) mapping process, grid momentum update, and grid-to-particle (G2P) mapping process in each time step. With the expansion of the calculation scale, especially when considering the spatial variability of strength for layered slope and conducting large-scale MCSs, the calculation

amount and time cost of the conventional CPU-based RMPM increase significantly, becoming the main bottleneck in practical applications.

As the widespread application of GPUs in the field of scientific computing, GPU-based parallel acceleration technology has provided a new solution for large-scale numerical simulation [48]. Compared to CPUs, GPUs are specifically designed for highly parallel computation. They feature a large number of cores, reduced thread scheduling overhead, and significantly higher memory bandwidth. Leveraging the Compute Unified Device Architecture (CUDA) developed by NVIDIA, modern desktop GPUs can simultaneously activate thousands of processing cores, while also offering flexible and efficient memory management mechanisms. It is friendly to MPM that uses particles and nodes as basic operation objects and has a highly data-parallel computing mode.

To improve the computational efficiency of large-deformation analyses that incorporate spatial variability and layered slope system, a parallel design and optimization strategy is implemented for the core computational procedures of MPM. In conventional CPU-based implementations, the mapping operations between material points and background grid nodes are performed serially in a cyclic manner, which becomes computationally expensive when a large number of material points and MCSs are involved. In contrast, the GPU architecture enables these operations to be executed in parallel, thereby significantly improving computational efficiency. The proposed GPU-RMPM framework decomposes each simulation step into several parallel computing modules. These primarily include: (1) parallelization of the particle-to-grid (P2G) mapping process, (2) parallel solution of the momentum conservation equations at grid nodes, and (3) parallelization of the grid-to-particle (G2P) mapping process.

Parallelization of P2G

In the MPM, P2G mapping is to transfer the physical quantities (such as mass, momentum, and force) carried by particles to the background grids. This process is the key bridge connecting particle description and grid calculation. The P2G mapping include: 1) contribute particle mass and momentum to nodal mass (m_I) and nodal momentum ($m\boldsymbol{v}$)$_I$; 2) contribute particle internal force (caused by stress) to nodal internal force, f_I^{int}. 3) contribute particle external force to nodal external force, f_I^{ext}. In each time step, the P2G process can be expressed as the following formulas.

$$m_I = \sum_p m_p N_I(x_p) \quad (1516\backslash* \text{MERGEFORMAT}())$$

$$(mv)_I = \sum_p m_p v_p N_I(x_p) \quad (1718\backslash* \text{MERGEFORMAT}())$$

$$f_I^{int} = -\sum_p V_p \sigma_p \nabla N_I(x_p) \quad (1920\backslash* \text{MERGEFORMAT}())$$

$$f_I^{ext} = \sum_p m_p b_p N_I(x_p) + \sum_p V_p t_p N_I(x_p) h^{-1} \quad (2122\backslash* \text{MERGEFORMAT}())$$

$N_I(\boldsymbol{x}_p)$ denotes the value of the GIMP shape function evaluated at the particle position $\boldsymbol{x}_p$. m_p and $\boldsymbol{v}_p$ are the mass and velocity of the particle respectively. $\boldsymbol{b}_p$ is the body force and $\boldsymbol{t}_p$ is the face force of the particle. h denotes the boundary height. Figure 1 shows the difference of the P2G process on CPU and GPU method, using a four-node cell as illustration.

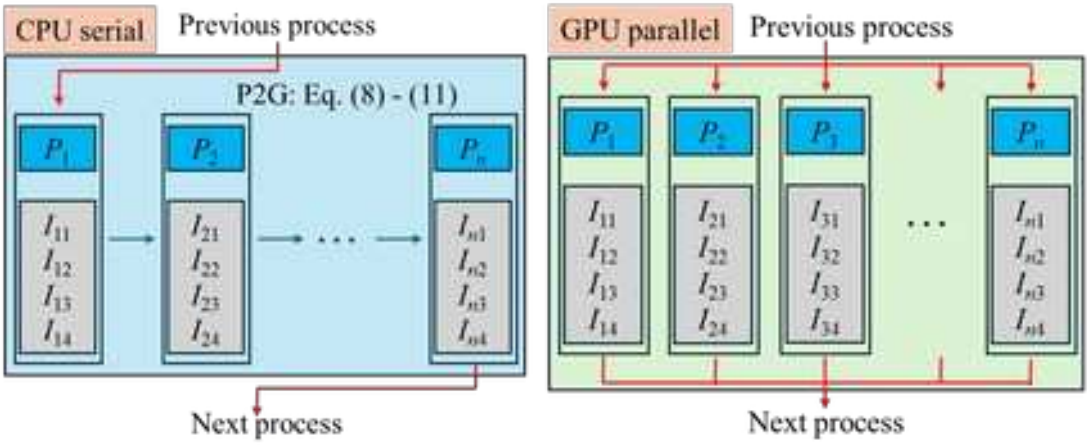

(a) (b)

Figure 1 The P2G mapping process. (a) CPU-serial; (b) GPU-parallel.

Parallel Solution of the Momentum Conservation at Grid

This study adopts the explicit solver of MPM. Therefore, the nodal acceleration $\boldsymbol{a}_I$ and velocity $\boldsymbol{v}_I$ are updated based on the m_I and force as follows.

$$a_I^{t+\Delta t/2} = \frac{1}{m_I}\left(f_I^{ext} + f_I^{int}\right) \quad (2324\backslash* \text{MERGEFORMAT}())$$

$$\boldsymbol{v}_i^{t+\Delta t/2} = \frac{1}{m_i}\left[(m\boldsymbol{v})_i + (\boldsymbol{f}_i^{ext} + \boldsymbol{f}_i^{int})\Delta t\right] \quad 2526\text{* MERGEFORMAT ()}$$

where Δt is the time increment.

Figure 2 shows the difference of the grid momentum update process on CPU and GPU method.

Parallelization of G2P

The G2P mapping process is to map the updated information on the background grids back to the particles, thereby updating the material points information. The G2P mapping process includes: 1) update particles position; 2) update particles velocity; 3) update particles strain and stress. In each time step, the G2P process can be expressed as follows.

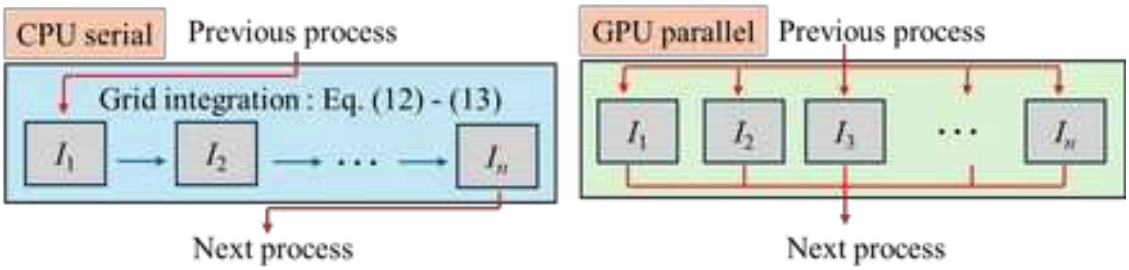

(a) (b)

Figure 2 The grid momentum update process. (a) CPU-serial; (b) GPU-parallel.

$$\boldsymbol{v}_p^{t+\Delta t} = \boldsymbol{v}_p^t + \sum_i N_i(\boldsymbol{x}_p)\boldsymbol{a}_i^{t+\Delta t/2}\Delta t \quad 2728\text{* MERGEFORMAT ()}$$

$$\boldsymbol{x}_p^{t+\Delta t} = \boldsymbol{x}_p^t + \sum_i N_i(\boldsymbol{x}_p)\boldsymbol{v}_i^{t+\Delta t/2}\Delta t \quad 2930\text{* MERGEFORMAT ()}$$

$$\Delta\boldsymbol{\varepsilon} = \frac{1}{2}(\boldsymbol{L} + \boldsymbol{L}^T)\Delta t \quad 3132\text{* MERGEFORMAT ()}$$

$$\Delta\boldsymbol{\omega} = \frac{1}{2}(\boldsymbol{L} - \boldsymbol{L}^T)\Delta t \quad 3334\text{* MERGEFORMAT ()}$$

where $\Delta\boldsymbol{\varepsilon}$ is the strain increment tensor, $\Delta\boldsymbol{\omega}$ is the spin increment tensor, $\boldsymbol{L}$ is the velocity gradient

$$L = \nabla \cdot \boldsymbol{v}_p = \frac{\partial \boldsymbol{v}_p}{\partial \boldsymbol{x}} = \sum_i \boldsymbol{v}_i \otimes N_i(\boldsymbol{x}_p)$$ 3536* MERGEFORMAT ()

The stress $\boldsymbol{\sigma}$ at time $t + \Delta t$ can be obtained by integrating the Cauchy stress rate $\dot{\boldsymbol{\sigma}}$

$$\boldsymbol{\sigma}(t + \Delta t) = \boldsymbol{\sigma}(t) + \dot{\boldsymbol{\sigma}} \Delta t$$ 3738* MERGEFORMAT ()

Since the material derivative of the Cauchy stress tensor is affected by the rotation of the rigid body and is not an objective tensor, the Jaumann stress rate $\boldsymbol{\sigma}^{\nabla}$ should be used in the constitutive relation. The relationship between $\dot{\boldsymbol{\sigma}}$ and $\boldsymbol{\sigma}^{\nabla}$ is

$$\dot{\boldsymbol{\sigma}} \Delta t = \boldsymbol{\sigma}^{\nabla} \Delta t - \Delta \boldsymbol{\omega} \cdot \boldsymbol{\sigma} + \boldsymbol{\sigma} \cdot \Delta \boldsymbol{\omega}$$ 3940* MERGEFORMAT ()

where

$$\boldsymbol{\sigma}^{\nabla} \Delta t = \boldsymbol{D} : \Delta \boldsymbol{\varepsilon}$$ 4142* MERGEFORMAT ()

$\boldsymbol{D}$ is the tangential stiffness matrix defined by the constitutive model. In this study, the Drucker-Prager (DP) elastoplastic constitutive model is used. In geotechnical engineering applications, the DP model with non-associative flow rules can be used to describe the behavior of geotechnical materials, which is characterized by three parameters: φ, c, and dilatation angle (ψ). The yield function $f(\boldsymbol{\sigma})$ and plastic potential function $g(\boldsymbol{\sigma})$ of this model can be expressed as follows, respectively.

$$f(\boldsymbol{\sigma}) = \begin{cases} q_\varphi \sigma_m + \sqrt{J_2} - k_c & \text{, shear yield} \\ \sigma_m - \sigma_t & \text{, tensile yield} \end{cases}$$ 4344* MERGEFORMAT ()

$$g(\boldsymbol{\sigma}) = \begin{cases} q_\psi \sigma_m + \sqrt{J_2} & \text{, shear yield} \\ \sigma_m & \text{, tensile yield} \end{cases}$$ 4546* MERGEFORMAT ()

where σ_t is tensile strength and mean stress $\sigma_m = I_1/3$. I_1 and J_2 are stress invariants. q_φ, k_c, and q_ψ are defined as follows.

$$q_\varphi = \frac{3 \tan \varphi}{\sqrt{9 + 12 \tan^2 \varphi}}$$ 4748* MERGEFORMAT ()

$$k_{\psi'} = \frac{3c}{\sqrt{9 + 12\tan^2\psi'}} \qquad 4950\text{* MERGEFORMAT ()}$$

$$q_{\psi'} = \frac{3\tan\psi'}{\sqrt{9 + 12\tan^2\psi'}} \qquad 5152\text{* MERGEFORMAT ()}$$

Figure 3 shows the difference of the G2P process on CPU and GPU method.

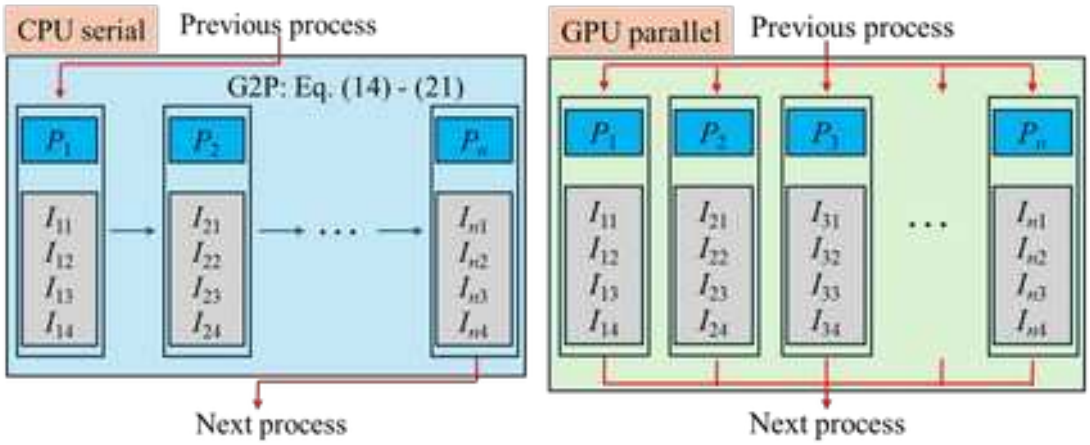

(a) (b)

Figure 3 The G2P mapping process. (a) CPU-serial; (b) GPU-parallel.

Therefore, the overall workflow of the proposed GPU-RMPM framework is illustrated in Figure 4. The main procedures can be summarized as follows:

1. Define the model input parameters, including slope geometry and the statistical properties of soil strength parameters, such as mean value, COV, marginal probability distribution, autocorrelation function, and scale of fluctuation.
2. Based on the prescribed statistical properties, generate N realizations of spatially variable random fields. The generated random fields are then mapped onto the material points of the MPM model.
3. Perform large-deformation simulations for each random field realization using the GPU-RMPM. First, set $k = 1$. Then the index is updated as $k = k + 1$ for each simulation. The procedure is repeated until $k = N$.
4. Identify the failure modes associated with post-failure slope, and extract the corresponding post-failure behaviors, including influence range and sliding volume. Determine the best-fit probability distributions and evaluate the associated statistical characteristics of the post-failure behaviors.

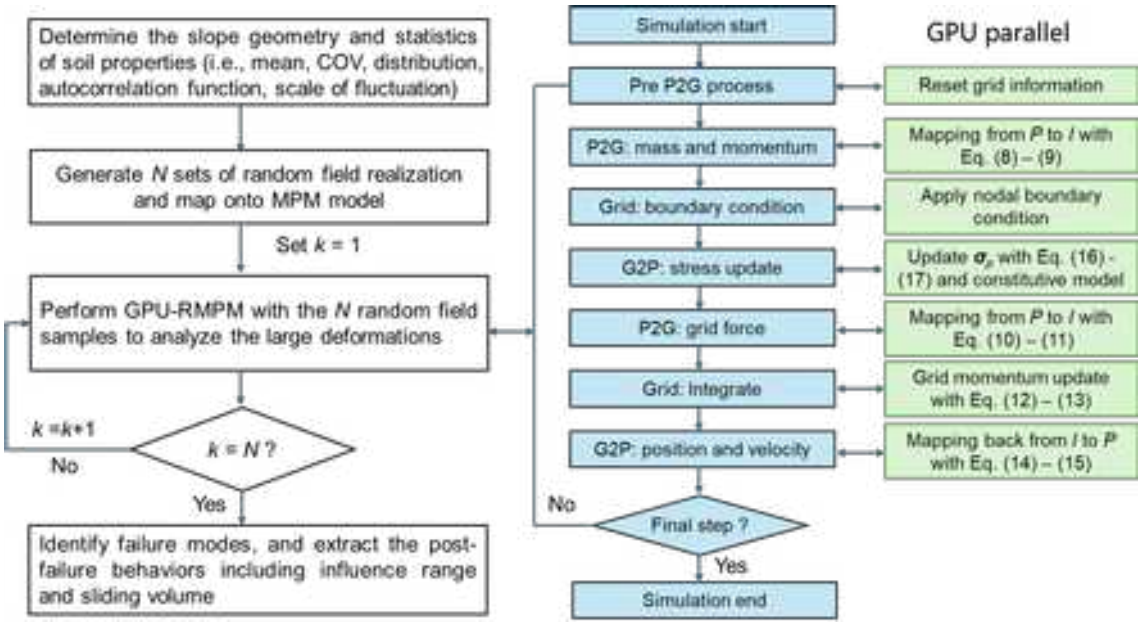

Figure 4 The workflow of GPU-RMPM.

Large-deformation analysis of layered slope

To analyze the large deformation of post-failure slope in layered soil systems, a representative example is adopted based on the two-layer soil slope model proposed by Deng et al. [6]. As illustrated in Figure 5, the slope has a height of 10 m and a slope ratio of 1:1. In the initial configuration of the MPM model, a structured background grid composed of square elements with a length of 0.2 m is employed. Particles are spaced at 0.1 m intervals, with four particles assigned to each grid cell. The base of the model is constrained with a fixed boundary condition, while roller boundaries are applied to the lateral.

Prior to initiating the large deformation, a gravitational loading step is carried out to establish the initial stress equilibrium. Subsequently, the slope undergoes failure and transitions into a gravity-driven landslide runout process. The total simulation time is set to 10 s with $\Delta t = 1.0 \times 10^{-4}$, allowing full observation of the failure initiation, movement, and final deposition.

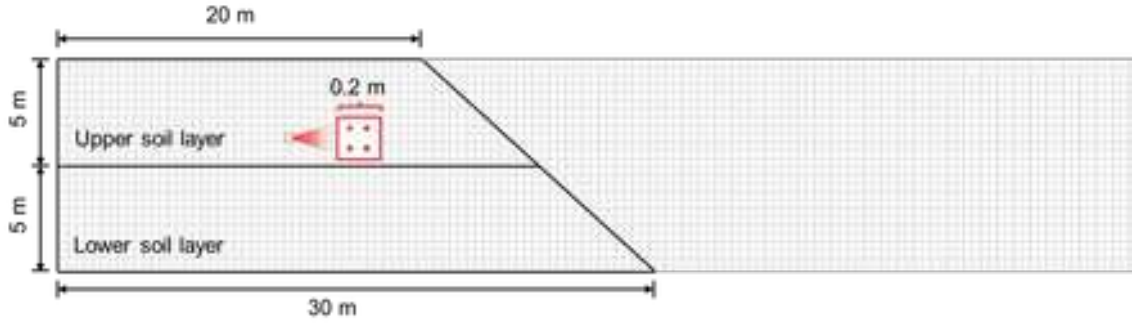

Figure 5 Geometry of the two-layer slope.

Deterministic analysis

In this section, a deterministic analysis is adopted to numerically investigate the post-failure behaviors of the homogeneous slope. The material properties of the two-layer slope are summarized in Table 1. The upper and lower soil layers share identical basic physical parameters: Young's modulus E = 20 MPa, Poisson's ratio v = 0.3, and unit weight γ = 18 kN/m^3. For strength parameters, the c of the upper layer is set to 4 kPa, while that of the lower layer is 8 kPa; the φ of the upper layer is set to 15°, while that of the lower layer is 30°. The ψ is set to 0° for both layers. These strength parameters represent a relatively weak slope condition, allowing slope failure and subsequent large deformation to occur in the simulations [16,19,31].

To evaluate the post-failure behaviors of the landslide quantitatively, two key metrics are introduced in this study: influence range and sliding volume, as shown in Figure 6. First, particles with a relative displacement greater than 0.4 m are identified as the sliding mass, serving as the basis for delineating the extent of the landslide [53]. Once the sliding mass is determined, the two metrics are defined as follows: influence range is the horizontal distance between the newly formed rear scarp and the furthest sliding mass; sliding volume is calculated by multiplying the number of sliding masses by their initial particle volume.

Table 1 The material parameters for two-layer slope.

Soil properties	Value	
	Upper soil layer	Lower soil layer
γ (kN/m^3)	18	
E (MPa)	20	
v	0.3	

dilatation angle, ψ(°)		0	
Cohesion, c (kPa)	4		8
Internal friction angle, φ(°)	15		30

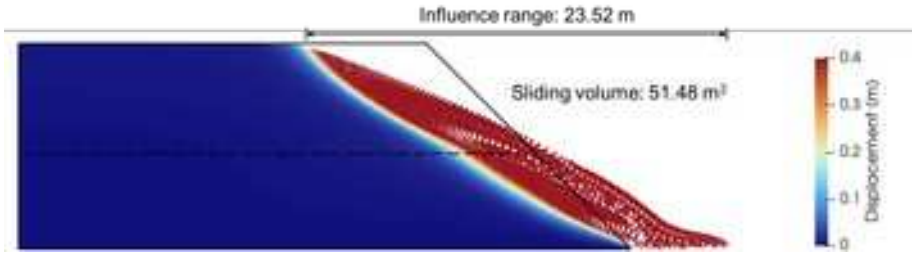

Figure 6 The final configuration of MPM simulation.

Figure 6 presents the final deposition configuration obtained from the MPM simulation, corresponding to a homogeneous slope. At t = 6.0 s, the movement has effectively ceased, with the landslide no longer undergoing significant deformation, indicating that the system has reached a stable state. Based on the configuration of the sliding masses, the resulting influence range is measured as 23.52 m and sliding volume as 51.48 m^2. These results provide a fundamental reference for the subsequent probabilistic analyses and sensitivity analyses.

Probabilistic analysis

In natural geological environments, soil strength properties—such as c and φ—exhibit pronounced spatial variability due to inherent geological and depositional processes [50,54]. To realistically simulate large-deformation landslide processes, it is therefore essential to explicitly account for this spatial variability in numerical analyses. This section systematically investigates the effects of spatial variability and parameter sensitivity—including θ_h, COV, β, and $R_{c\varphi}$—on the post-failure behaviors and failure modes of the studied layered slopes. To ensure physical realism and avoid nonphysical negative values, both c and φ are modeled as lognormally distributed random fields. The statistical properties adopted for the representative slope, including mean value, COV, scale of fluctuation (horizontal θ_h and vertical θ_v), β, and $R_{c\varphi}$, are summarized in Table 2. The mean strength parameters are selected to be consistent with the deterministic analysis (Table 1), thereby enabling direct comparison between homogeneous and spatially variable conditions. The adopted COV values (0.3 for c and 0.2 for φ) fall within commonly reported ranges in the

literature [55]. The θ_h = 20.0 m and θ_v = 2.0 m are chosen based on typical values reported for natural soil deposits [16,54]. The $R_{c\varphi}$ and β are set to 0, corresponding to statistically independent strength parameters and non-rotated anisotropy, which act as a reference case for subsequent parametric studies to evaluate their impact on post-failure landslide responses.

Table 2 The statistical properties for probabilistic analysis.

Parameter	Mean value		COV	θ_h (m)	θ_v (m)	$R_{c\varphi}$	β (°)
Cohesion, c (kPa)	Upper soil layer	4	0.3	20.0	2.0	0.0	0
	Lower soil layer	8					
Internal friction angle, φ (°)	Upper soil layer	15	0.2				
	Lower soil layer	30					

To quantify the uncertainty associated with the post-failure behaviors of slopes, the convergence of the MCSs is first examined using the random field parameters summarized in Table 2. The cumulative mean values and standard deviations (SD) of influence range and sliding volume are evaluated as functions of the number of MCSs, based on a total of 2000 realizations of spatially variable random fields. As shown in Figure 7(a), the cumulative mean values of the post-failure behaviors exhibit clear convergence trends. Specifically, after approximately 400 simulations, the mean values stabilize, indicating statistical convergence. The final statistics yield a mean influence range of 22.67 m with a 95% confidence interval (CI) of ±0.15 m, and a mean sliding volume of 50.72 m^2 with a 95% CI of ±0.44 m^2. Figure 7(b) further illustrates the evolution of the SDs with increasing numbers of MCSs. Consistent with the convergence behavior of the cumulative mean values, the SDs approach stable values after approximately 400 simulations, providing additional evidence for the robustness of the probabilistic estimates. The SD of the influence range is 3.36 m, while the SD of the sliding volume is 10.06 m^2. Based on these observations, 2000 MCSs are adopted for each parametric case in the subsequent analyses to ensure both numerical stability and statistical reliability. Therefore, including all cases in the sensitivity analysis, a total of 38000 MCSs are performed in this study.

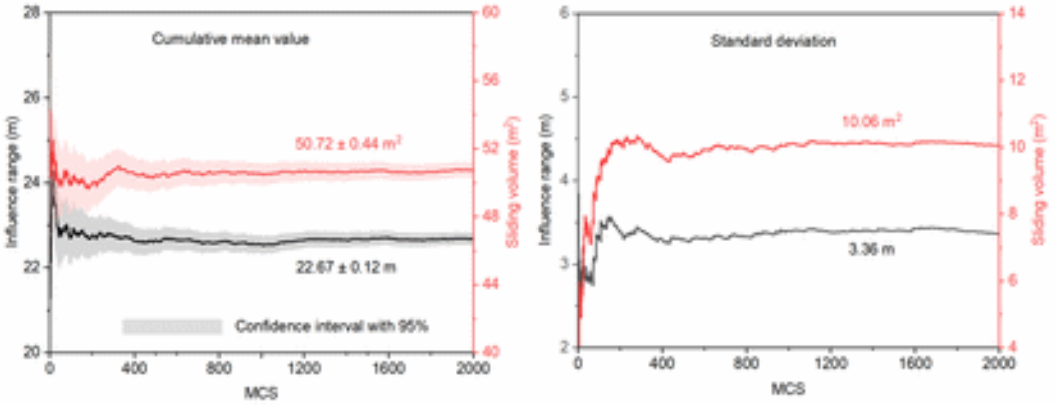

(a) (b)

Figure 7 The evolution of post-failure behaviors with MCSs. (a) Cumulative mean value; (b) SD.

Due to the presence of spatial variability in soil strength, slope failure mechanisms are no longer characterized by a single, deterministic failure mode as commonly observed in homogeneous slopes. Instead, depending on the spatial distribution of strength parameters within the random fields, distinct failure modes may develop during large-deformation analyses [20,24]. As illustrated in Figure 8, the sliding volumes of the lower soil layer obtained from the 2000 MCSs using the parameters in Table 2 are statistically analyzed. The resulting histogram exhibits a clear separation between two groups of realizations. One group of realizations is concentrated in the range smaller than 1.0 m^2, indicating that sliding is essentially confined to the upper soil layer, while the lower layer remains largely stable. In contrast, another group is distributed within the range of 4.0-22.0 m^2, indicating that significant sliding occurs in the lower soil layer and that both soil layers are mobilized during the landslide process. Based on this observation, two representative slope failure modes at large deformation are identified according to the sliding volume of the lower soil layer. When the sliding volume of the lower soil layer is smaller than 1.0 m^2, the failure mode is classified as Local Failure (LF). Otherwise, the failure mode is classified as Global Failure (GF).

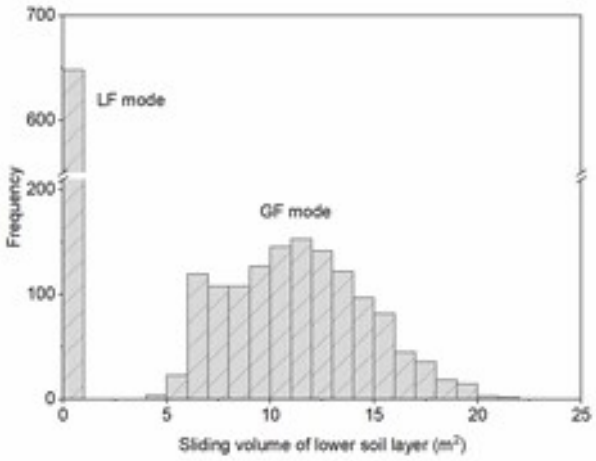

Figure 8 The histogram of sliding volume of lower soil layer.

Figures 9(a)-(b) present the spatial distributions of c and φ for a representative LF realization, while Figure 9(c) shows the corresponding large-deformation failure mechanism. In this case, the random field realization reveals a continuous low-strength zone predominantly within the upper soil layer, whereas the lower layer retains relatively higher strength. This localized weak band provides a preferential path for shear localization and effectively inhibits downward propagation of the failure surface, thereby confining deformation to the upper layer. In contrast, Figures 10(a)-(b) display the spatial distributions of c and φ for a representative GF realization, and Figure 10(c) presents the associated failure mechanism. Here, low-strength regions extend from the upper layer into the lower layer, forming a vertically connected weak zone. Such connectivity allows shear localization to propagate downward across the layer interface, resulting in mobilization of both soil layers and the development of a deeper and more extensive sliding mass. For the homogeneous slope considered in this study (Figure 6), only the GF mode is observed. In the absence of spatial variability, strength distribution within each layer is uniform, and no localized weak zones exist to alter the failure path, leading exclusively to the GF mode. When spatial variability in strength parameters is introduced according to Table 2, however, failure mode becomes realization-dependent. Among the 2000 large-deformation MCSs, 548 cases exhibit LF mode, whereas 1352 cases correspond to GF mode. These results indicate that the connectivity and distribution of low-strength zones affect energy dissipation and strain localization, thereby influencing failure mode development in layered slopes.

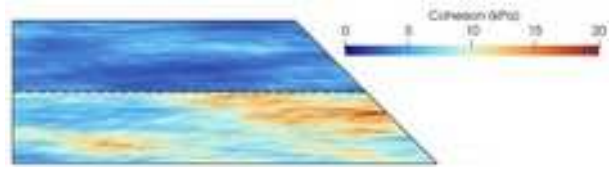

(a)

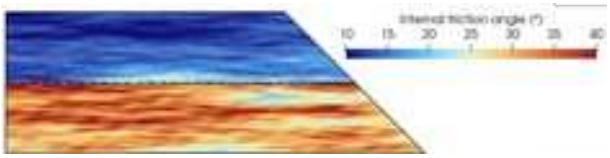

(b)

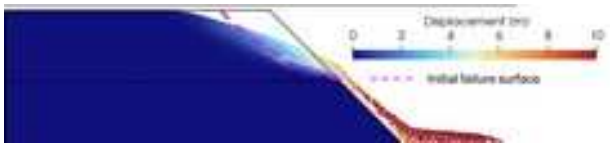

(c)

Figure 9 The typical spatial distribution of soil strength together with the corresponding failure mode for LF mode. (a) Typical distribution of cohesion for LF mode; (b) Typical distribution of internal friction angle for LF mode; (c) Typical LF mode.

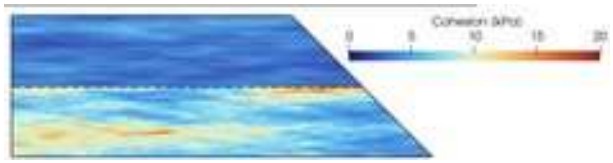

(a)

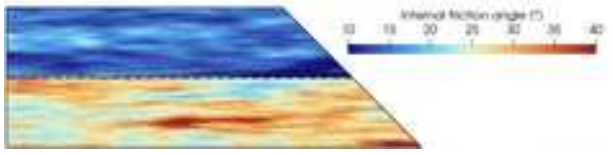

(b)

(c)

Figure 10 The typical spatial distribution of soil strength together with the corresponding failure mode for GF mode. (a) Typical distribution of cohesion for GF mode; (b) Typical distribution of internal friction angle for GF mode; (c) Typical GF mode.

In large-deformation analyses, the post-failure behaviors of slopes are strongly dependent on the failure modes. Figure 11 presents a scatter plot illustrating the relationship between influence range and sliding volume for the two identified failure modes. For the LF mode, data points are predominantly clustered in the lower-left region of the plot, whereas those corresponding to the GF mode are mainly distributed toward the upper-right region. To further clarify the statistical characteristics of the data distribution, the influence range is divided into three percentile intervals based on the overall dataset, namely 0-5%, 5-95%, and 95-100%. Within the lowest 0-5% interval, most cases correspond to the LF mode. In contrast, within the highest 95-100% interval, most cases correspond to the GF mode. For the central 5-95% interval, which contains the majority of realizations, both failure modes occur with similar probability in this influence range region. Specifically, 89.2% of LF cases and 93.3% of GF cases fall within this interval. However, even under comparable influence ranges, the sliding volumes associated with the GF mode are generally larger than those corresponding to the LF mode.

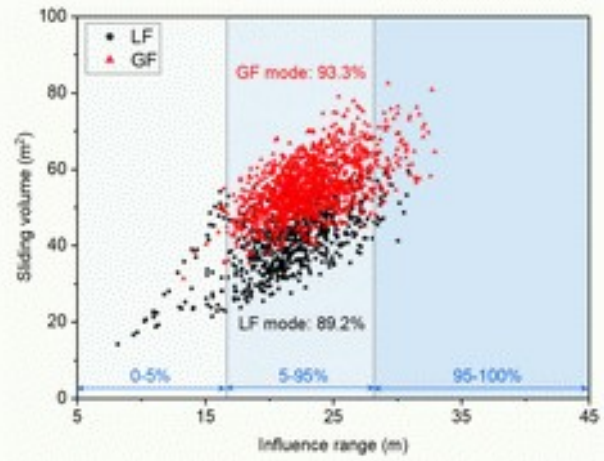

Figure 11 The relationship between influence range and sliding volume.

Further insights are provided by the histograms of Figure 12 classified by failure mode. For landslides experiencing LF mode, the sliding volume is primarily distributed within the range of 14.18-61.02 m^2, while the corresponding influence range spans approximately 7.58-31.14 m. In contrast, landslides characterized by GF mode display markedly larger sliding volume, predominantly ranging from 31.42-82.50 m^2, with influence range locating

between 13.28-33.45 m. These results demonstrate that the failure mode exerts a dominant influence on the sliding volume. Moreover, the goodness-of-fit of the influence range and sliding volume for each failure mode is evaluated using the Kolmogorov-Smirnov (K-S) test. The results show that the *P*-values for normality (P_{normal}) are greater than 0.05. Therefore, the null hypothesis of normal distribution cannot be rejected at the 95% confidence level, indicating that both the influence range and sliding volume data can be reasonably described by normal distributions.

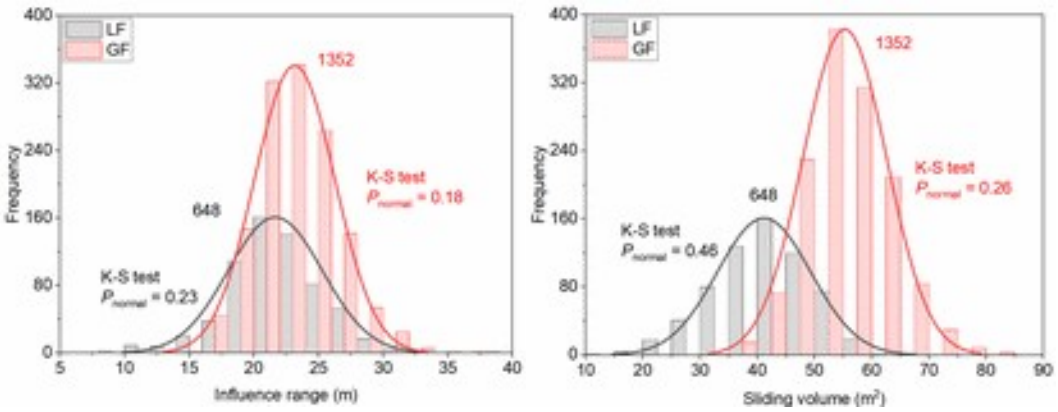

(a) (b)

Figure 12 The distribution of post-failure behaviors classified by failure mode. (a) Influence range; (b) Sliding volume.

The underlying mechanism can be attributed to the distinct post-failure behaviors of the two failure modes. In the LF mode, landslides are governed by shallow and relatively thin sliding masses confined to the upper soil layer, resulting in limited sliding volume and relatively shallow failure depth. In contrast, the GF mode involves mobilization of both soil layers, producing a substantially thicker sliding mass and a deeper failure surface, and consequently a significantly larger sliding volume. Although the influence ranges of the two failure modes may be comparable, the sliding volume and failure depth associated with the GF mode are consistently greater than those of the LF mode. As a result, slope failures occurring in the GF mode generally impose more severe post-failure consequences. This difference highlights the necessity of distinguishing between the two failure modes. In practice, stratified slopes are commonly encountered in natural and engineered environments [56,57]. Depending on the spatial distribution of soil strength, either LF or GF may develop. From an engineering perspective, these two failure modes differ substantially in terms of hazard magnitude and required mitigation measures. Misidentifying a GF case as an LF case may lead to significant underestimation of landslide consequences and inappropriate design of prevention strategies. Therefore, distinguishing between LF and GF provides a meaningful and engineering-relevant basis for

probabilistic post-failure hazard assessment.

Parameter sensitivity analysis

Effect of θ_h

The scale of fluctuation characterizes the spatial continuity of soil strength and directly controls the connectivity of weak zones within layered slopes. In practical geotechnical investigations, soil properties often exhibit stronger spatial correlation in the horizontal direction than in the vertical direction. Variations in θ_h have important implications for failure surface development, post-failure deformation, and hazard severity [8,16]. Consequently, this section focuses on examining how θ_h influences probabilistic post-failure consequences of slopes [58]. Seven horizontal scales of fluctuation are considered, θ_h = 2.0, 3.0, 4.0, 20.0, 500.0, 1000.0 and 2000.0 m, while all other parameters are adopted from Table 2.

Figure 13(a) illustrates the probability density histogram of the influence range with θ_h = 20.0 m. The influence range is plotted along the horizontal axis, while the vertical axis represents the probability density. Both normal (red line) and log-normal (black line) distribution functions are fitted to the numerical results, and their goodness-of-fit are evaluated using the K-S test. The K-S test return the P_{normal} is 0.12, while the P-value of lognormal distribution ($P_{lognormal}$) is less than 0.05, indicating that the normal distribution hypothesis of influence range data cannot be rejected at the 95% confidence level. The mean influence range is 22.67 m with a SD of 3.36 m, compared to 23.52 m obtained from the deterministic analysis (dashed line). This discrepancy indicates substantial variability induced by spatial heterogeneity and suggests that deterministic analysis may underestimate the potential landslide impact, thereby highlighting the importance of incorporating spatial variability in large-deformation analysis. Figure 13(b) compares the fitted normal probability density functions (PDFs) for all considered θ_h. As θ_h increases from 2.0 m to 20.0 m, the PDF curves become progressively flatter and wider, indicating increasing dispersion and a higher likelihood of extreme influence range. However, when θ_h is further increased from 20.0 m to 2000.0 m, the PDF curves become concentrated. The box plot in Figure 13(c) further quantifies these trends, showing that the mean value, SD and 1%-99% ranges of the influence range increase gradually as θ_h increases from 2.0 m to 20.0 m. In contrast, for θ_h increases from 500.0 m to 2000.0 m, the influence range converges toward the deterministic result, while the SD decreases significantly.

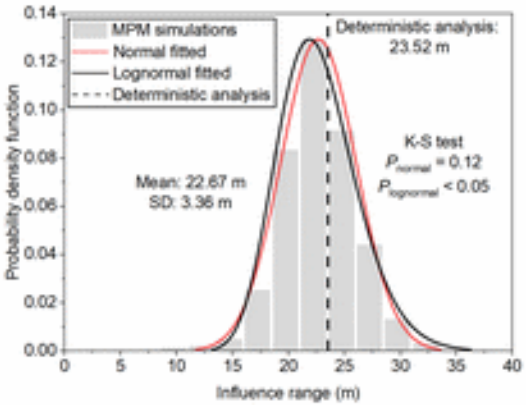

(a)

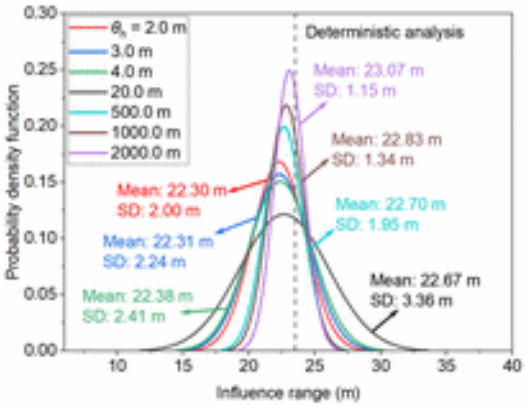

(b)

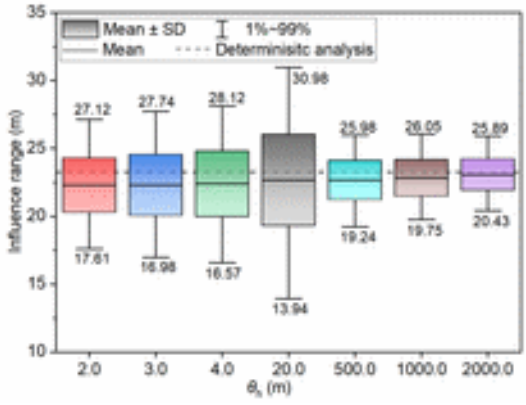

(c)

Figure 13 The distribution of influence range.(a) Histogram with θ_h = 20.0 m; (b) The fitted normal PDF curves for different θ_h; (c) Box diagram for different θ_h.

Similarly, Figure 14(a) presents the probability density histogram of the sliding volume with θ_h = 20.0 m. The histogram is fitted with both normal (red line) and log-normal (black line) PDFs. Consistent with influence range, the

P_{normal} of K-S test shows that the observed sliding volume data cannot be rejected normal distribution. The mean sliding volume is 50.72 m^2, which is similar to the deterministic result of 51.48 m^2. Figure 14(b) compares the fitted normal PDFs of sliding volume for different θ_h. As θ_h increases from 2.0 m to 20.0 m, the probability density curves become progressively flatter and wider, reflecting increased dispersion and a greater likelihood of extreme sliding volumes. The corresponding box plot in Figure 14(c) further illustrates the evolution of statistical characteristics, showing that the SD and 1%-99% ranges of sliding volume increase with θ_h over the range from 2.0 m to 20.0 m. However, when θ_h is further increased from 500.0 to 2000.0 m, the SD and 1%-99 % ranges decrease to a relatively low level, and the MCS results become increasingly concentrated around the deterministic analysis.

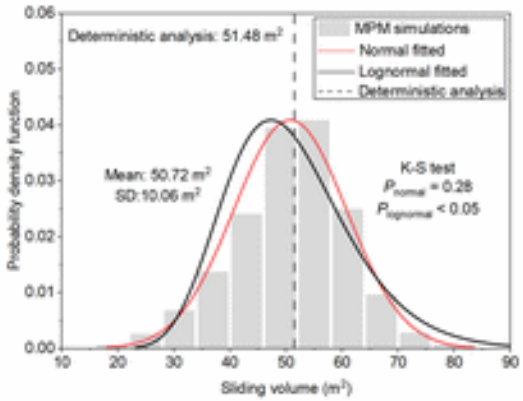

(a)

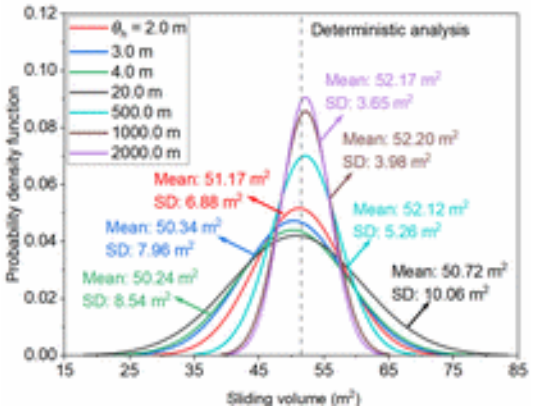

(b)

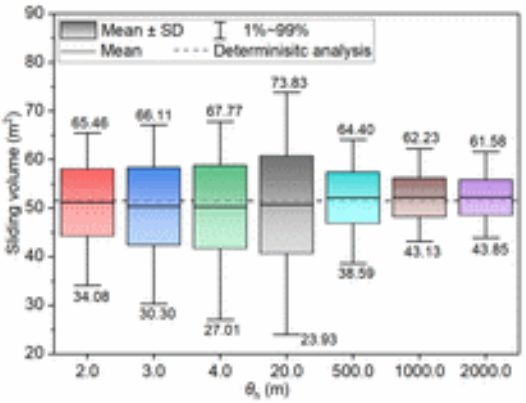

(c)

Figure 14 The distribution of sliding volume.(a) Histogram with θ_h = 20.0 m; (b) The fitted normal PDF curves for different θ_h; (c) Box diagram for different θ_h.

By synthesizing the results presented in Figures 13-14, it can be observed that within a moderate range of horizontal fluctuation lengths (e.g., θ_h = 2.0-20.0 m), increasing θ_h leads to broader probability distributions and enhanced dispersion in both influence range and sliding volume. This behavior reflects the increasing spatial continuity of strength, which amplifies realization-dependent variability in post-failure behaviors. This implies that slopes with moderately correlated horizontal strength structures may exhibit greater uncertainty in landslide consequences, thereby increasing the likelihood of extreme post-failure scenarios. In contrast, when θ_h becomes sufficiently large (e.g., θ_h = 2000.0 m, approximately 200 times the slope height), the spatial variability within each realization becomes nearly uniform over the slope domain. In this situation, the probabilistic response converges toward the deterministic solution. This observation highlights that the most critical range of θ_h for probabilistic hazard assessment is neither extremely small nor extremely large, but rather within an intermediate regime where strength heterogeneity is spatially continuous enough to alter failure mode competition while still maintaining substantial randomness.

As shown in Figure 15, the evolution of failure modes with increasing θ_h exhibits a non-monotonic trend. When θ_h increases within a moderate range (2.0-20.0 m), the proportion of LF increases because the limited spatial continuity of weak zones in the relatively stronger lower layer inhibits the downward propagation of the failure surface, leading to a higher occurrence of the LF mode. However, when θ_h increases to large values (500.0-2000.0 m), weak zones in the lower layer become increasingly continuous within the slope, facilitating deeper failure propagation and resulting in the dominance of the GF mode. This non-monotonic behavior indicates that θ_h plays a

governing role in failure mode selection by controlling the spatial connectivity of strength heterogeneity.

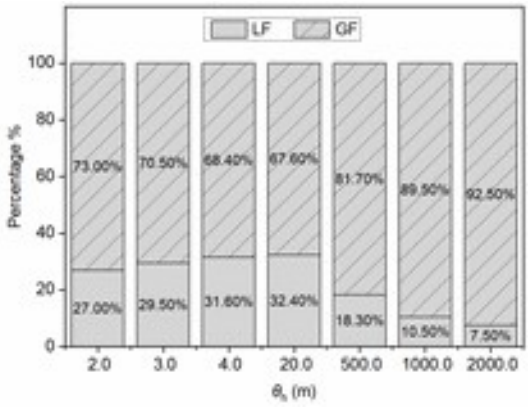

Figure 15 The evolution of failure modes with θ_h.

Overall, the results demonstrate that θ_h not only influences the statistical dispersion of post-failure behaviors but also fundamentally regulates failure mechanism competition in layered slopes. Therefore, reliable stochastic large-deformation analysis requires careful consideration of horizontal scale of fluctuations.

Effect of COV

The COV reflects the intensity of spatial variability and is directly related to the level of uncertainty in site investigation and parameter estimation. In practical engineering applications, COV depends on geological complexity, sampling density, and data interpretation methods [54]. Therefore, understanding its influence on post-failure behaviors is essential for evaluating how uncertainty in soil characterization propagates into landslide hazard predictions. In the reference case, the COV of c and φ are taken as 0.3 and 0.2, respectively. To quantitatively evaluate the sensitivity of the results to variability intensity, the COVs of both c and φ are systematically scaled upward and downward by a factor of 0.8 relative to the reference values, while all other parameters are kept unchanged. The resulting combinations of COVs for the shear strength parameters are summarized in Table 3.

Table 3 The determination of COV values for c and φ.

Parameter	COV_1	COV_2	COV_3	COV_4	COV_5
COV for c	0.192	0.24	0.3	0.375	0.46875
COV for φ	0.128	0.16	0.2	0.25	0.3125

Figures 16(a) and (b) present the fitted normal PDFs of influence range and sliding volume for different COVs.

The results clearly demonstrate that COV exerts a pronounced effect on both post-failure behaviors. Increasing COV leads to a systematic increase in both the mean values and SDs of the influence range and sliding volume. Correspondingly, the PDFs become wider and more flattened, indicating enhanced dispersion and a higher likelihood of extreme outcomes. For example, when COV increases from COV_1 to COV_5, the mean sliding volume increases from 49.12 m^2 to 55.74 m^2, while the SD more than doubles from 6.79 m^2 to 14.57 m^2. These results indicate that variability intensity not only enlarges expected landslide consequences but also substantially amplifies uncertainty. In addition, Figure 16(c) shows the variation in failure mode proportions with increasing COV. A slight increase in the occurrence of the GF mode is observed as COV increases.

Overall, the results highlight that COV fundamentally controls both the magnitude and dispersion of post-failure behaviors. From an engineering perspective, underestimating COV may lead to non-conservative predictions of landslide consequences, whereas higher variability levels require more cautious design considerations.

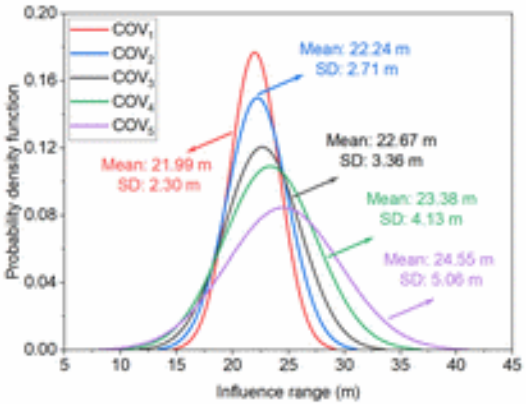

(a)

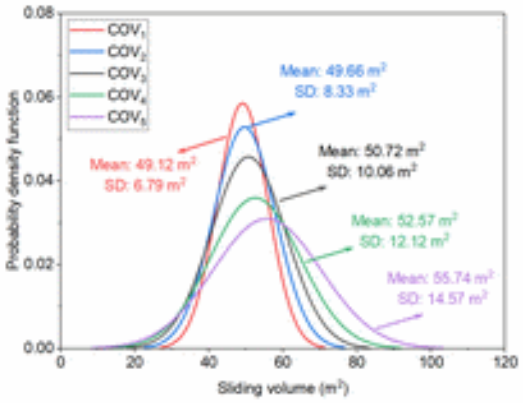

(b)

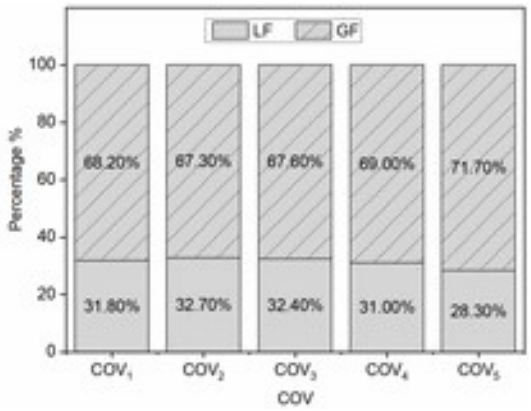

(c)

Figure 16 The distribution of post-failure behaviors and failure modes with various COVs. (a) Influence range; (b) Sliding volume; (c) The distribution of failure modes.

Effect of β

The β characterizes the principal direction of spatial correlation in the random field and controls the preferential orientation of strength continuity within the slope. In natural deposits, soil fabric and geological structures often introduce directional anisotropy into mechanical properties. Therefore, examining the effect of β is essential for understanding how the orientation of strength heterogeneity influences landslide consequences. In the reference configuration, β is set to 0°, corresponding to horizontally aligned spatial correlation. In this section, five anisotropy rotation angles are considered, namely β = -45°, -22.5°, 0°, 22.5°, and 45°, while all other parameters are adopted from Table 2. Figures 17(a) and (b) present typical realizations of the rotated random fields corresponding to β = -45° and β = 45°, respectively.

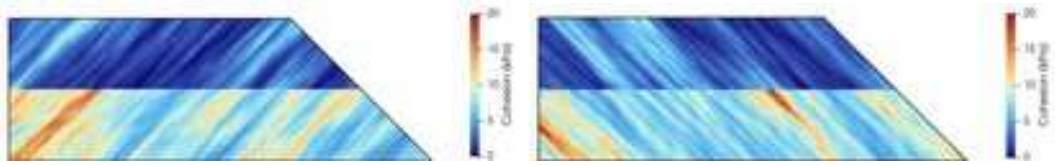

(a) (b)

Figure 17 The typical random field realization of β. (a) β = -45°; (b) β = 45°.

Figures 18(a) and (b) compare the fitted normal PDFs of influence range and sliding volume for the different β. The results indicate that the rotation angle of anisotropy exerts a noticeable influence on both post-failure behaviors.

The PDF curves of sliding volume become progressively wider and flatter as β increases, indicating an increase in the SD and thus enhanced variability. This trend suggests that rotated anisotropy promotes greater dispersion in the sliding volume. The effect of β on the mean values of influence range and sliding volume, however, exhibits a non-monotonic pattern. Specifically, for the set of β = -22.5°, 0°, and 22.5°, the mean values increase as β increases. In contrast, when considering β = -45° and 45°, the mean values of both influence range and sliding volume decrease with increasing β. In addition, the influence of anisotropy rotation on failure mode occurrence is illustrated in Figure 18(c). As β increases from -45° to 45°, the proportion of LF cases increases from 30% to 35%. As a result, the orientation of geological structures or depositional fabric may either promote or inhibit the development of continuous weak zones along potential slip directions. Therefore, neglecting anisotropy orientation in probabilistic analysis may overlook unfavorable structural alignments that amplify landslide consequences.

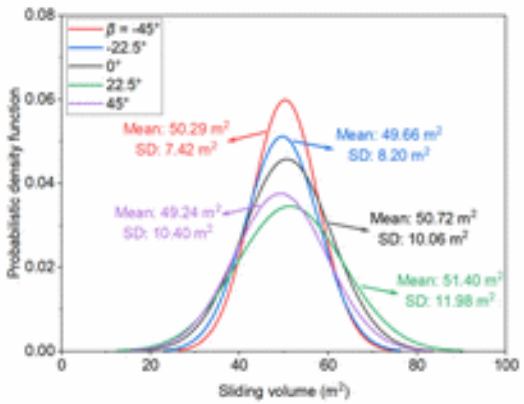

(a)

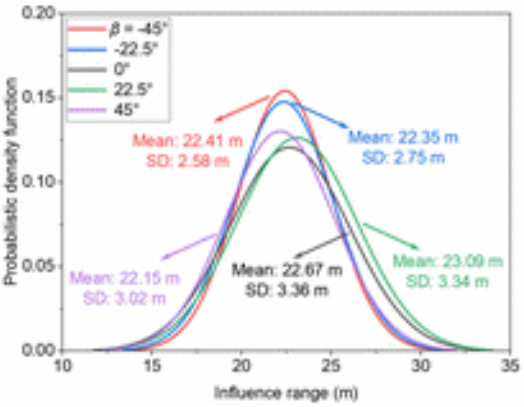

(b)

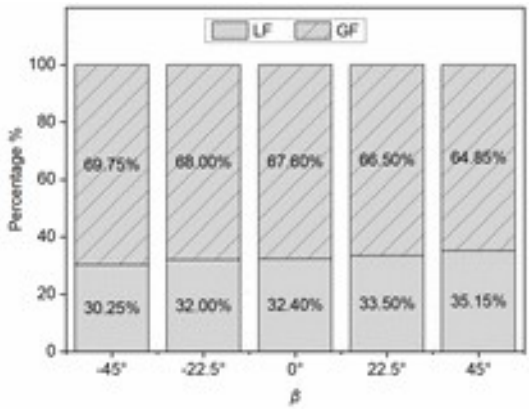

(c)

Figure 18 The distribution of post-failure behaviors and failure modes with various β. (a) Influence range; (b) Sliding volume; (c) The distribution of failure modes.

Effect of $R_{c\varphi}$

The $R_{c\varphi}$ governs the degree to which local fluctuations in these two strength parameters occur simultaneously. In natural soils, c and φ may exhibit statistical dependence due to common depositional history or stress history. Therefore, investigating the influence of $R_{c\varphi}$ is essential for understanding how coupled strength variability affects post-failure landslide consequences. Five values of $R_{c\varphi}$ are examined in this study, namely -0.5, -0.25, 0, 0.25, and 0.5, following the ranges commonly adopted in previous studies [55,59].

Figures 19(a) and (b) present the fitted normal PDFs of influence range and sliding volume for different values of $R_{c\varphi}$. The results indicate that increasing $R_{c\varphi}$ leads to systematic increases in both the mean values and the dispersion of the post-failure behaviors. Specifically, as $R_{c\varphi}$ increases, the PDF curves become wider, flatter, and shift progressively to the right, indicating larger expected influence ranges and sliding volumes, as well as increased uncertainty. For example, when $R_{c\varphi}$ = -0.5, the influence range varies between 10.48-32.71 m, with a mean value of 22.20 m and a SD of 2.43 m. When $R_{c\varphi}$ increases to 0.5, the influence range expands to 7.78-39.22 m, accompanied by an increased mean of 23.16 m and a SD of 4.03 m. These results demonstrate that positive cross-correlation between c and φ significantly increases the probability of extreme scenarios. In addition, Figure 19(c) illustrates the influence of $R_{c\varphi}$ on the occurrence of failure modes. As $R_{c\varphi}$ increases, the proportion of GF cases exhibits a decreasing trend, indicating that stronger positive cross-correlation tends to suppress thicker sliding masses under the investigated conditions.

Overall, it is evident that increasing the $R_{c\varphi}$ amplifies both the mean values and variances of post-failure

behaviors. In practical terms, neglecting the statistical cross-correlation between c and φ may lead to a significant underestimation of landslide potential impacts. When c and φ are negatively correlated, the predicted outcomes are relatively conservative, whereas positive cross-correlation tends to yield slightly non-conservative estimates of post-failure impacts. These findings highlight the necessity of incorporating cross-correlation effects in stochastic large-deformation analyses.

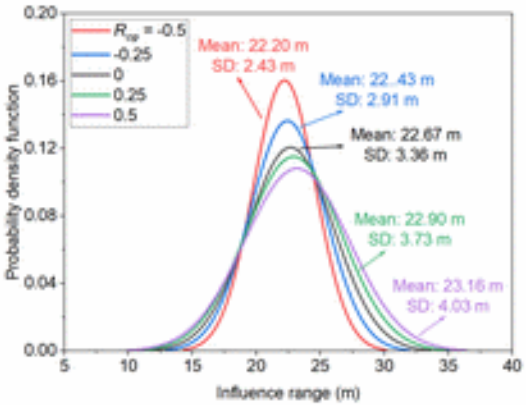

(a)

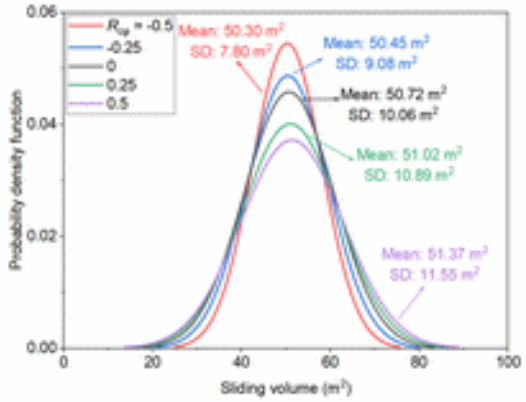

(b)

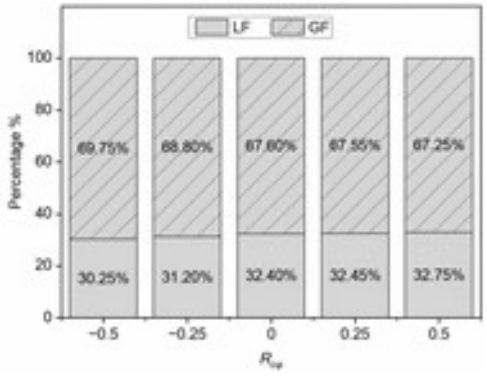

(c)

Figure 19 The distribution of post-failure behaviors and failure modes with various $R_{c\varphi}$. (a) Influence range; (b) Sliding volume; (c) The distribution of failure modes.

Comparison of Computational Efficiency

In previous studies on stochastic large-deformation analyses, numerical computations have primarily relied on CPU-based serial processing [60]. When high-resolution particle discretization is required to represent the structure of spatial variability accurately and large-scale MCSs to ensure convergence of probabilistic measures, traditional CPU methods often result in excessive computational cost and prolonged simulation times. This significantly hampers the efficiency and feasibility of large-scale stochastic analyses. To overcome these limitations, a GPU-RMPM is adopted in this study to simulate post-failure large-deformation processes. All simulations are performed using an NVIDIA RTX 3080 Ti GPU. For comparison purposes, the same numerical framework is also executed on a conventional CPU platform (Intel Ultra5-245KF), allowing a direct evaluation of the computational performance gains achieved through GPU acceleration.

Table 4 presents a comparison of representative computation times between the present study and previously published CPU-based simulations. Qu et al. [59] reported an average computation time of approximately 26.8 min per simulation using a CPU, with 14,310 particles and a mesh size of 0.5 m. Similarly, Liu et al. [24] employed 14,336 particles with a mesh size of 1.0 m and reported computation times of approximately 18.0 min per simulation on a personal computer and 2.8 min on a high-performance computing platform. In the present study, the proposed GPU-RMPM framework is implemented with a total of 49,990 material points, which is approximately three times the number of particles adopted in the aforementioned studies. Despite this substantial increase in spatial resolution, the average computation time per simulation is reduced to approximately 0.6 min. For reference, when the same model is executed using a CPU (Intel Ultra5-245KF), the average computation time is approximately 5.8 min per simulation.

Table 4 The time consumption of calculating random field sample.

Mesh size	Number of particles	Processor	Calculation time per simulation (min)	Reference
0.5	14310	CPU	26.8	Qu et al. [59]

1.0	14336	CPU	18.0 and 2.8	Liu et al. [24]
0.2	49900	GPU	0.6	This study
		CPU	5.8	

This corresponds to a computational speedup of approximately 9.67 times achieved by the GPU-accelerated implementation. This improvement highlights the efficiency of the GPU-accelerated implementation in handling stochastic large-deformation analyses involving spatially variable random fields.

Conclusion

To elucidate how the inherent heterogeneity of soils within natural slopes—characterized by both stratification and spatial variability of material properties—governs post-failure landslide hazards, this study investigates the post-failure behaviors and failure modes of two-layer slope considering coupled c-φ spatial variability. A GPU-RMPM framework is developed to enable large-scale probabilistic simulations. The effects of parameter sensitivity—including θ_h, COV, β, and $R_{c\varphi}$—on post-failure behaviors and failure modes are systematically examined. Based on the overall findings of this study, the following conclusions are drawn:

1. Failure mode exerts a dominant control on post-failure sliding volume. For a comparable influence range, GF mode mobilizes a larger sliding volume than LF mode due to the involvement of thicker and deeper sliding masses.
2. Horizontal heterogeneity significantly affects post-failure variability. Moderate increases in horizontal fluctuation length amplify both the mean values and dispersion of influence range and sliding volume, whereas sufficiently large fluctuation lengths lead to homogenized behavior with reduced variability and a predominant GF mode.
3. Increasing the COV of shear strength parameters enlarges both the expected magnitude and uncertainty of post-failure behaviors and promotes the occurrence of GF, highlighting the non-conservative nature of deterministic analyses.
4. Positive cross-correlation between c and φ increases the mean values and variability of post-failure behaviors, thereby elevating the probability of extreme scenarios, while negative correlation yields comparatively

conservative predictions.

5. The proposed GPU-RMPM framework significantly improves computational efficiency, achieving an approximately tenfold speedup over conventional CPU-based approaches and enabling practical large-scale stochastic large-deformation analyses of slopes with strength spatial variability.

Acknowledgments

The authors appreciate the financial support from the National Natural Science Foundation of China (Grant Nos. 42472335, W2521142, 42572352, 52278413).

References

[1] Guo S, Griffiths DV. Failure mechanisms in two-layer undrained slopes. Can Geotech J 2020; 57:1617-21. https://doi.org/10.1139/cgj-2019-0642.

[2] Lim K, Li AJ, Lyamin AV. Three-dimensional slope stability assessment of two-layered undrained clay. Comput Geotech 2015;70:1-17. https://doi.org/10.1016/j.compgeo.2015.07.011.

[3] Zhou H, Hu Q, Yu X, Zheng G, Liu X, Xu H, et al. Quantitative bearing capacity assessment of strip footings adjacent to two-layered slopes considering spatial soil variability. Acta Geotech 2023;18:6759-73. https://doi.org/10.1007/s11440-023-01875-8.

[4] Li AJ, Merifield RS, Lyamin AV. Limit analysis solutions for three dimensional undrained slopes. Comput Geotech 2009;36:1330-51. https://doi.org/10.1016/j.compgeo.2009.06.002.

[5] Qian ZG, Li AJ, Merifield RS, Lyamin AV. Slope Stability Charts for Two-Layered Purely Cohesive Soils Based on Finite-Element Limit Analysis Methods. Int J Geomech 2015;15:06014022. https://doi.org/10.1061/(ASCE)GM.1943-5622.0000438.

[6] Deng D, Li L. Failure modes and a calculation method for a stability analysis on a layered slope with a focus on interlayer sliding. Arabian J Geosci 2019;12:182. https://doi.org/10.1007/s12517-019-4308-1.

[7] Liu K, Wang YQ, Huang M, Yuan WH. Postfailure Analysis of Slopes by Random Generalized Interpolation Material Point Method. Int J Geomech 2021;21:04021015. https://doi.org/10.1061/(ASCE)GM.1943-5622.0001953.

[8] Wang B, Hicks MA, Vardon PJ. Slope failure analysis using the random material point method. Géotech Lett 2016;6:113-8. https://doi.org/10.1680/jgele.16.00019.

[9] Griffiths DV, Fenton GA. Probabilistic Slope Stability Analysis by Finite Elements. J Geotech Geoenviron Eng 2004;130:507-18. https://doi.org/10.1061/(ASCE)1090-0241(2004)130:5(507).

[10] Wu C, Wang ZZ, Goh SH, Zhang W. Comparing 2D and 3D slope stability in spatially variable soils using random finite-element method. Comput Geotech 2024;170:106324. https://doi.org/10.1016/j.compgeo.2024.106324.

[11] Liang Y, Jia Z, Wu Q, Xiao K, Yuan R, Zhou H, et al. Probabilistic slope stability analysis based on the Hermite-logistic regression approach. Adv Eng Software 2025;208:103973. https://doi.org/10.1016/j.advengsoft.2025.103973.

[12] Ma G, Rezania M, Nezhad MM. Effects of spatial autocorrelation structure for friction angle on the runout distance in heterogeneous sand collapse. Transp Geotech 2022;33:100705. https://doi.org/10.1016/j.trgeo.2021.100705.

[13] Liu X, Wang Y. Probabilistic simulation of entire process of rainfall-induced landslides using random finite element and material point methods with hydro-mechanical coupling. Comput Geotech 2021;132:103989. https://doi.org/10.1016/j.compgeo.2020.103989.

[14] Zhang W, Ji J, Gao Y, Li X, Zhang C. Spatial variability effect of internal friction angle on the post-failure behavior of landslides using a random and non-Newtonian fluid based SPH method. Geosci Front 2020;11:1107-21. https://doi.org/10.1016/j.gsf.2020.02.003.

[15] Zhang W, Zhang W, Chen Y, Ji J, Gao Y. Uncertainty evaluation of the run-out distance of flow-like landslides considering the anisotropic scale of fluctuation in the random field of internal friction angle. Acta Geotech 2023;18:5839-57. https://doi.org/10.1007/s11440-023-02041-w.

[16] Bi Z, Wu W, Zhang L, Peng C. Uncertainty Analysis of Post-Failure Behavior in Landslides Based on SPH Method and Generalized Geotechnical Random Field Theory. Comput Geotech 2024;171:106363. https://doi.org/10.1016/j.compgeo.2024.106363.

[17] Zhu H, Zhang LM. Characterizing geotechnical anisotropic spatial variations using random field theory. Can Geotech J 2013;50:723-34. https://doi.org/10.1139/cgj-2012-0345.

[18] Bi Z, Wu W, Zhang L, Peng C. Efficient Random Field Generation With Rotational Anisotropy for Probabilistic SPH Analysis of Slope Failure. Int J Numer Anal Methods Geomech 2024;48:4520-38. https://doi.org/10.1002/nag.3858.

[19] Li J-P, Jiang S-H, Ma G-T, Rezania M, Mousavi Nezhad M, Wan J-H. Probabilistic evaluation of landslide influence zones considering stratigraphic dips and nonstationarity of soil properties. Computers and Geotechnics 2025;177:106815. https://doi.org/10.1016/j.compgeo.2024.106815.

[20] Jiang S-H, Li J-P, Ma G, Rezania M, Huang J. Stochastic hazard assessment framework of landslide blocking river by depth-integrated continuum method and random field theory. Landslides 2024. https://doi.org/10.1007/s10346-024-02347-0.

[21] He Y, Yu J, Yuan R, Wang W, Nikitas N. Stability and failure mechanisms in three-dimensional cracked slope: Static and dynamic analysis. Computers and Geotechnics 2022;144:104626. https://doi.org/10.1016/j.compgeo.2021.104626.

[22] He Y, Yu J, Yuan R, Nikitas N. 3D modeling-based area-volume power-law relationships for incipient rotational slides. Geomorphology 2023;441:108885. https://doi.org/10.1016/j.geomorph.2023.108885.

[23] Ng CWW, Qu C, Cheung RWM, Guo H, Ni J, Chen Y, et al. Risk assessment of soil slope failure considering copula-based rotated anisotropy random fields. Comput Geotech 2021;136:104252. https://doi.org/10.1016/j.compgeo.2021.104252.

[24] Liu X, Wang Y, Li DQ. Investigation of slope failure mode evolution during large deformation in spatially variable soils by random limit equilibrium and material point methods. Comput Geotech 2019;111:301-12. https://doi.org/10.1016/j.compgeo.2019.03.022.

[25] Zhang W, Wu Z, Peng C, Li S, Dong Y, Yuan W. Modelling large-scale landslide using a GPU-accelerated 3D MPM with an efficient terrain contact algorithm. Comput Geotech 2023;158:105411. https://doi.org/10.1016/j.compgeo.2023.105411.

[26] Yuan W-H, Liu K, Zhang W, Dai B, Wang Y. Dynamic modeling of large deformation slope failure using smoothed particle finite element method. Landslides 2020;17:1591-603. https://doi.org/10.1007/s10346-020-

01375-w.

[27] Cho SE. Effects of spatial variability of soil properties on slope stability. Eng Geol 2007;92:97-109. https://doi.org/10.1016/j.enggeo.2007.03.006.

[28] He Y, Li Z, Ou J, Yuan R. Random Finite-Element Analysis of Slope Considering Strength Anisotropy and Spatial Variability of Soil. Nat Hazard Rev 2024;25:04024010. https://doi.org/10.1061/NHREFO.NHENG-2000.

[29] Yuan R, Jia Z, Sun J, Ou J, Wang W, He Y, et al. Probabilistic Analysis of a Three-Dimensional Slope Based on Limit Analysis. Nat Hazard Rev 2024;25:04024043. https://doi.org/10.1061/NHREFO.NHENG-2093.

[30] Li DQ, Xiao T, Cao ZJ, Phoon KK, Zhou CB. Efficient and consistent reliability analysis of soil slope stability using both limit equilibrium analysis and finite element analysis. Appl Math Modell 2016;40:5216-29. https://doi.org/10.1016/j.apm.2015.11.044.

[31] Ma G, Rezania M, Nezhad MM. Stochastic Assessment of Landslide Influence Zone by Material Point Method and Generalized Geotechnical Random Field Theory. Int J Geomech 2022;22:04022002. https://doi.org/10.1061/(ASCE)GM.1943-5622.0002308.

[32] Bui HH, Fukagawa R, Sako K, Ohno S. Lagrangian meshfree particles method (SPH) for large deformation and failure flows of geomaterial using elastic-plastic soil constitutive model. Int J Numer Anal Methods Geomech 2008;32:1537-70. https://doi.org/10.1002/nag.688.

[33] Ma Y, Asai M, Han Z, Chen G. Two-layer multi-state SPH modelling of momentum growth and its feedback in viscous debris flow on wet bed sediment. Eng Geol 2024;343:107804. https://doi.org/10.1016/j.enggeo.2024.107804.

[34] Peng C, Wu W, Yu H, Wang C. A SPH approach for large deformation analysis with hypoplastic constitutive model. Acta Geotech 2015;10:703-17. https://doi.org/10.1007/s11440-015-0399-3.

[35] Singh V, Peng C, Islam MRI. Three-dimensional SPH modeling of brittle fracture under hydrodynamic loading. Comput Fluids 2025;301:106763. https://doi.org/10.1016/j.compfluid.2025.106763.

[36] Zhang B, Li W, Pu J, Bi Y, Huang Y. Centrifuge and DEM investigation of dry granular impacts: Effect of granular volume under high-speed impact conditions. Landslides 2024;21:1439-59. https://doi.org/10.1007/s10346-024-02219-7.

[37] Yerro A, Girardi V, Martinelli M, Ceccato F. Modelling unsaturated soils with the Material Point Method. A discussion of the state-of-the-art. Geomech Energy Environ 2022;32:100343. https://doi.org/10.1016/j.gete.2022.100343.

[38] Liang Y, Chandra B, Soga K. Shear band evolution and post-failure simulation by the extended material point method (XMPM) with localization detection and frictional self-contact. Comput Methods Appl Mech Eng 2022;390:114530. https://doi.org/10.1016/j.cma.2021.114530.

[39] Lu M, Ceccato F, Zhou M, Yerro A, Zhang J. Evaluating the exceedance probability of the runout distance of rainfall-induced landslides using a two-stage FEM-MPM approach. Acta Geotech 2023. https://doi.org/10.1007/s11440-023-02160-4.

[40] Kasama K, Furukawa Z, Hu L. Practical reliability analysis for earthquake-induced 3D landslide using stochastic response surface method. Comput Geotech 2021;137:104303. https://doi.org/10.1016/j.compgeo.2021.104303.

[41] Hu LH, Takahashi A, Kasama K. Effect of spatial variability on stability and failure mechanisms of 3D slope using random limit equilibrium method. Soils Found 2022;62:101225. https://doi.org/10.1016/j.sandf.2022.101225.

[42] Zhou Q, Xu W-J, Dong X-Y. SPH-DEM coupling method based on GPU and its application to the landslide tsunami. Part I: method and validation. Acta Geotech 2022;17:2101-19. https://doi.org/10.1007/s11440-021-01388-2.

[43] Hu L, Zhang R, Wang G, Li Y, Li Z, Li F, et al. Variance reduction function modeling for a potential circular slip surface in spatially variable slopes. Engineering Geology 2026;365:108636. https://doi.org/10.1016/j.enggeo.2026.108636.

[44] Zhang W, Gu X, Hong L, Han L, Wang L. Comprehensive review of machine learning in geotechnical reliability analysis: Algorithms, applications and further challenges. Applied Soft Computing 2023;136:110066. https://doi.org/10.1016/j.asoc.2023.110066.

[45] Liu X, Liu Y, Yang Z, Li X. A novel dimension reduction-based metamodel approach for efficient slope reliability analysis considering soil spatial variability. Computers and Geotechnics 2024;172:106423. https://doi.org/10.1016/j.compgeo.2024.106423.

[46] Li P, Jin Y-F, Chen X. Active learning of slope failure probability considering soil spatial variability by Bayesian compressive sensing and K-weighted-means clustering. Georisk: Assessment and Management of Risk for Engineered Systems and Geohazards 2025;0:1-20. https://doi.org/10.1080/17499518.2025.2531851.

[47] Wang ZZ, Zhang J, Huang H. Interpreting random fields through the U-Net architecture for failure mechanism and deformation predictions of geosystems. Geosci Front 2024;15:101720. https://doi.org/10.1016/j.gsf.2023.101720.

[48] Peng C, Wang S, Wu W, Yu H, Wang C, Chen J. LOQUAT: an open-source GPU-accelerated SPH solver for geotechnical modeling. Acta Geotech 2019;14:1269-87. https://doi.org/10.1007/s11440-019-00839-1.

[49] Zhao J, Chen Y, Zhang H, Xia H, Wang Z, Peng Q. Physically based modeling and animation of landslides with MPM. Vis Comput 2019;35:1223-35. https://doi.org/10.1007/s00371-019-01709-3.

[50] Vanmarcke EH. Probabilistic Modeling of Soil Profiles. J Geotech Eng Div 1977;103:1227-46. https://doi.org/10.1061/AJGEB6.0000517.

[51] Li L, Wang Y, Cao Z. Probabilistic slope stability analysis by risk aggregation. Eng Geol 2014;176:57-65. https://doi.org/10.1016/j.enggeo.2014.04.010.

[52] Sulsky D, Chen Z, Schreyer HL. A particle method for history-dependent materials. Comput Methods Appl Mech Eng 1994;118:179-96. https://doi.org/10.1016/0045-7825(94)90112-0.

[53] Wang Y, Qin Z, Liu X, Li L. Probabilistic analysis of post-failure behavior of soil slopes using random smoothed particle hydrodynamics. Eng Geol 2019;261:105266. https://doi.org/10.1016/j.enggeo.2019.105266.

[54] Phoon K-K, Kulhawy FH. Characterization of geotechnical variability. Can Geotech J 1999;36:612-24. https://doi.org/10.1139/t99-038.

[55] Cho SE. Probabilistic Assessment of Slope Stability That Considers the Spatial Variability of Soil Properties. J Geotech Geoenviron Eng 2010;136:975-84. https://doi.org/10.1061/(ASCE)GT.1943-5606.0000309.

[56] Li D-Q, Zheng D, Cao Z-J, Tang X-S, Phoon K-K. Response surface methods for slope reliability analysis: Review and comparison. Eng Geol 2016;203:3-14. https://doi.org/10.1016/j.enggeo.2015.09.003.

[57] Ireland HO. Stability Analysis of the Congress Street Open Cut in Chicago. Geotechnique 1954;4:163-8. https://doi.org/10.1680/geot.1954.4.4.163.

[58] Huang HW, Xiao L, Zhang DM, Zhang J. Influence of spatial variability of soil Young's modulus on tunnel convergence in soft soils. Eng Geol 2017;228:357-70. https://doi.org/10.1016/j.enggeo.2017.09.011.

[59] Qu C, Wang G, Feng K, Xia Z. Large deformation analysis of slope failure using material point method with cross-correlated random fields. J Zhejiang Univ-SCI A 2021;22:856-69.

https://doi.org/10.1631/jzus.A2100196.

[60] Wang G, Li Y, Sun F, Zhang T, Wang R, Li B, et al. Probability Analysis of Landslide Large Deformation Characteristics Based on Copula-RMPM. Nat Hazard Rev 2025;26:04025028. https://doi.org/10.1061/NHREFO.NHENG-2385.